

# Detection of Wind Evolution and Lidar Trajectory Optimization for Lidar-Assisted Wind Turbine Control

DAVID SCHLIPF<sup>1\*</sup>, FLORIAN HAIZMANN<sup>1</sup>, NICOLAI COSACK<sup>2</sup>, TOM SIEBERS<sup>2</sup> and PO WEN CHENG<sup>1</sup>

<sup>1</sup>Stuttgart Wind Energy @ Institute of Aircraft Design

<sup>2</sup>KENERSYS GmbH

(Manuscript received August 18, 2014; in revised form March 13, 2015; accepted March 15, 2015)

## Abstract

Recent developments in remote sensing are offering a promising opportunity to rethink conventional control strategies of wind turbines. With technologies such as lidar, the information about the incoming wind field - the main disturbance to the system - can be made available ahead of time. Initial field testing of collective pitch feedforward control shows, that lidar measurements are only beneficial if they are filtered properly to avoid harmful control action. However, commercial lidar systems developed for site assessment are usually unable to provide a usable signal for real time control. Recent research shows, that the correlation between the measurement of rotor effective wind speed and the turbine reaction can be modeled and that the model can be used to optimize a scan pattern. This correlation depends on several criteria such as turbine size, position of the measurements, measurement volume, and how the wind evolves on its way towards the rotor. In this work the longitudinal wind evolution is identified with the line-of-sight measurements of a pulsed lidar system installed on a large commercial wind turbine. This is done by staring directly into the inflowing wind during operation of the turbine and fitting the coherence between the wind at different measurement distances to an exponential model taking into account the yaw misalignment, limitation to line-of-sight measurements and the pulse volume. The identified wind evolution is then used to optimize the scan trajectory of a scanning lidar for lidar-assisted feedforward control in order to get the best correlation possible within the constraints of the system. Further, an adaptive filter is fitted to the modeled correlation to avoid negative impact of feedforward control because of uncorrelated frequencies of the wind measurement. The main results of the presented work are a first estimate of the wind evolution in front of operating wind turbines and an approach which manufacturers of lidar systems can use to improve their devices to better assist preview control concepts.

**Keywords:** wind evolution, Longitudinal Spectral Coherence, lidar-assisted control

## 1 Introduction

The wind is not only the energy source for wind turbines but also the most important disturbance to the wind turbine control system. Thus, information about the wind inflow is valuable to optimize the energy production and reduce the structural loads. Lidar-assisted control has been widely investigated in recent years, addressing two coupled aspects: How can useful wind preview signals be extracted from lidar data? How can those signals be incorporated into the control strategy? A thorough understanding of the nature of the wind and measurement principles are mandatory for providing signals that enable successful preview control. This is a challenging application of remote sensing because of the limitations imposed by the lidar measurement principle and the complexity of the wind; the three-dimensional wind field is evolving due to the decay of turbulence structures and additionally disturbed by the operating turbine.

However, in initial field testing of lidar-assisted control on midscale research turbines by SCHOLBROCK *et al.* (2013) and SCHLIPF *et al.* (2014) positive results have

been achieved. In this work, the first findings of a follow-up experiment on a larger, commercial wind turbine are presented. The scan trajectory has been chosen such that a high correlation between the lidar measurement and the reaction of the wind turbine is obtained. As described by SCHLIPF *et al.* (2013a) and SIMLEY and PAO (2013a), this correlation depends not only on the scan configuration and lidar properties, but also on the rotor size and on the site-specific wind evolution.

The paper describes on the one hand, how the wind evolution is identified in the environment of an operating wind turbine with data from a staring lidar scan. On the other hand, the paper presents how the wind evolution is incorporated into a spectral correlation model. With this model a constrained optimization problem is solved to obtain a circular scan trajectory, which is able to provide the rotor effective wind speed with high correlation and before the measured wind reaches the rotor.

This paper is organized as follows. Section 2 presents the models used in the paper and Section 3 summarizes the experimental environment. In Section 4 the longitudinal decay parameter for the wind evolution model is estimated based on experimental data. The parameter is used in Section 5 to optimize a lidar system and conclusions and future work are discussed in Section 6.

\*Corresponding author: David Schlipf, Stuttgart Wind Energy @ Institute of Aircraft Design, University of Stuttgart, Germany, e-mail: David.Schlipf@ifb.uni-stuttgart.de

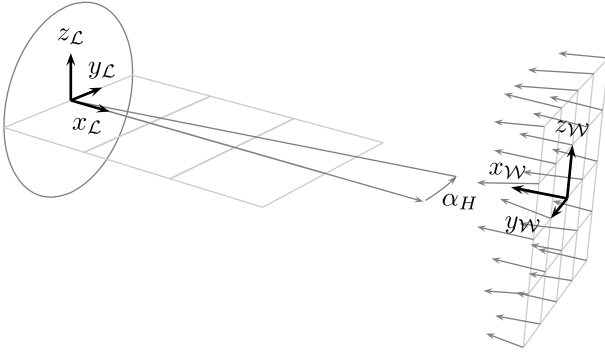


**Figure 1:** Used lidar ( $\mathcal{L}$ ) and wind ( $\mathcal{W}$ ) coordinate system. The origin of the  $\mathcal{W}$  is translated for better illustration.

## 2 Modeling

In this section, application specific models are presented. The wind and lidar models will be used in Section 4 to determine the wind evolution. In Section 5, the optimized scan trajectory is validated with the wind turbine model.

### 2.1 Wind modeling

The Kaimal turbulence model as defined in (IEC 61400-1, 2005) for neutral stratified atmosphere is used in this work to describe the turbulent three-dimensional wind vector in the wind coordinate system, see Figure 1. The wind coordinate system (subscript  $\mathcal{W}$ ) is aligned with the mean wind direction and thus yawed within the lidar coordinate system (subscript  $\mathcal{L}$ ) by the yaw misalignment  $\alpha_H$ . Within the wind coordinate system,  $u_{\mathcal{W}}$  is the longitudinal,  $v_{\mathcal{W}}$  the lateral, and  $w_{\mathcal{W}}$  the vertical component. The corresponding standard deviations for the Kaimal model are:

$$\sigma_u = I_{\text{ref}}(0.75\bar{u} + 5.6), \quad \sigma_v = 0.8\sigma_u, \quad \sigma_w = 0.5\sigma_u, \quad (2.1)$$

where  $\bar{u}$  is the mean longitudinal wind speed and the reference turbulence intensity  $I_{\text{ref}}$  for a high, medium, and low turbulence location is 16, 14, and 12 %. Normalized spectra for each velocity component  $h$  in a point  $i$  are given in the Kaimal model by

$$\frac{fS_{ii,h}}{\sigma_h^2} = \frac{4f\frac{L_h}{\bar{u}}}{\left(1 + 6f\frac{L_h}{\bar{u}}\right)^{(5/3)}}, \quad (2.2)$$

where the integral length scales  $L_h$  for each velocity component  $h$  with the turbulence scale parameter  $\Lambda_1 = 42$  m for hub heights over 60 m are:

$$L_u = 8.1\Lambda_1, \quad L_v = 2.7\Lambda_1, \quad L_w = 0.66\Lambda_1. \quad (2.3)$$

An important measure to describe the relation between two signals  $a$  and  $b$  is the coherence defined by

$$\gamma_{ab}^2 = \frac{|S_{ab}|^2}{S_{aa}S_{bb}}, \quad (2.4)$$

where  $S_{ab}$  is the cross spectrum, and  $S_{aa}$  and  $S_{bb}$  are the auto-spectra, respectively. The coherence is a function of frequency, where 0 indicates no correlation and 1 perfect correlation.

In the Kaimal model, the coherence  $\gamma_{ij,ur}^2$  of the longitudinal velocity component between two points  $i$  and  $j$  on a plane perpendicular to the mean wind direction with distance  $r_{ij}$  is modeled by

$$\gamma_{ij,ur}^2 = \exp(-2\kappa r_{ij})$$

$$\text{with } \kappa = 12 \sqrt{\left(\frac{f}{\bar{u}}\right)^2 + \left(\frac{0.12}{L_u}\right)^2}. \quad (2.5)$$

The Kaimal model assumes no correlation of the other two components for points with a separation of  $r_{ij} > 0$ . This is less realistic compared to other spectral models such as the one developed by MANN (1994), but will simplify the calculation in this paper significantly.

Wind evolution is considered here by a simple exponential model of coherence, as suggested by PIELKE and PANOFSKY (1970) and used by SIMLEY et al. (2012). The squared coherence between two points  $i$  and  $j$  with the longitudinal separation  $\Delta x_{ij,\mathcal{W}}$  is given by

$$\gamma_{ij,ux}^2 = \exp(-\alpha k \Delta x_{ij,\mathcal{W}}), \quad (2.6)$$

where  $\alpha$  is the dimensionless longitudinal decay parameter and  $k$  is the wavenumber. Other approaches such as the one presented by KRISTENSEN (1979) and used by BOSSANYI (2012) model the wind evolution in free stream based on physical considerations. However, their applicability for flow in front of an operating turbine needs to be validated. Therefore, the exponential model has been chosen over other models due to its simplicity.

### 2.2 Lidar system modeling

The lidar system model describes the wind speed measurement in the lidar ( $\mathcal{L}$ ) coordinate system. The relatively small movements of the lidar system due to the tower top displacement are not considered. The displacement of the lidar system from the hub has been considered in the calculations, but is not illustrated in this paper for simplicity.

A lidar system is only able to measure the component of the wind vector in the laser beam direction. Per convention, this value is positive, if the wind is directed towards the laser source. Therefore, the line-of-sight wind speed  $v_{\text{los},i}$  measured at point  $i$  with coordinates  $[x_{i,\mathcal{L}} \ y_{i,\mathcal{L}} \ z_{i,\mathcal{L}}]^T$  can be modeled by a projection of the wind vector  $[u_{i,\mathcal{L}} \ v_{i,\mathcal{L}} \ w_{i,\mathcal{L}}]^T$  at point  $i$  and the normalized vector of the laser beam. This is mathematically equivalent to the scalar product of both vectors:

$$v_{\text{los},i} = x_{ni,\mathcal{L}} u_{i,\mathcal{L}} + y_{ni,\mathcal{L}} v_{i,\mathcal{L}} + z_{ni,\mathcal{L}} w_{i,\mathcal{L}}. \quad (2.7)$$

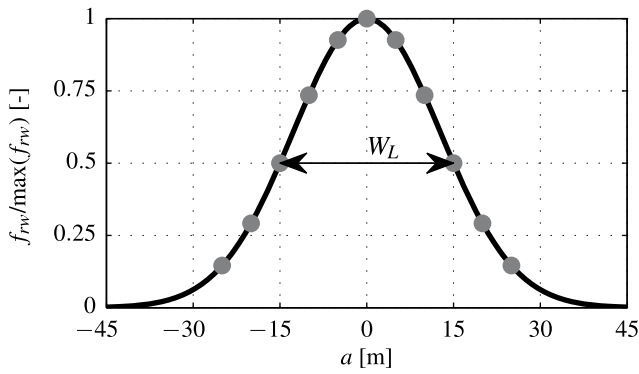


**Figure 2:** Normalized range weighting function  $f_{rw}$  for a pulsed lidar system (solid) and discrete values used in this analysis (dots).

Here, the normalized laser vector measuring at a distance  $r_i$  from the lidar system is defined by

$$\begin{bmatrix} x_{ni,\mathcal{L}} \\ y_{ni,\mathcal{L}} \\ z_{ni,\mathcal{L}} \end{bmatrix} = -\frac{1}{r_{Li}} \begin{bmatrix} x_{i,\mathcal{L}} \\ y_{i,\mathcal{L}} \\ z_{i,\mathcal{L}} \end{bmatrix}$$

with  $r_{Li} = \sqrt{x_{i,\mathcal{L}}^2 + y_{i,\mathcal{L}}^2 + z_{i,\mathcal{L}}^2}$ . (2.8)

The measurement coordinates and the wind vector can be transformed with the rotation matrix  $T_{W\mathcal{L}}$  by

$$\begin{bmatrix} u_{i,\mathcal{L}} \\ v_{i,\mathcal{L}} \\ w_{i,\mathcal{L}} \end{bmatrix} = \underbrace{\begin{bmatrix} -\cos(\alpha_H) & \sin(\alpha_H) & 0 \\ -\sin(\alpha_H) & -\cos(\alpha_H) & 0 \\ 0 & 0 & 1 \end{bmatrix}}_{T_{W\mathcal{L}}(\alpha_H)} \begin{bmatrix} u_{i,W} \\ v_{i,W} \\ w_{i,W} \end{bmatrix}. \quad (2.9)$$

In Equation (2.7) the measurement is assumed for one single point. However, real lidar systems measure within a probe volume due to the length of the emitted pulse for pulsed lidar systems. Further, the Fast Fourier Transform (FFT) involved in the detection of the frequency shift requires a certain length of time of the backscattered signal, contributing to the averaging effect. Thus, lidar measurements are modeled more realistically with the range weighting function  $f_{rw}(a)$  at the distance  $a$ :

$$v_{losV,i} = \int_{-\infty}^{\infty} (x_{ni,\mathcal{L}} u_{ai,\mathcal{L}} + y_{ni,\mathcal{L}} v_{ai,\mathcal{L}} + z_{ni,\mathcal{L}} w_{ai,\mathcal{L}}) f_{rw}(a) da. \quad (2.10)$$

The wind vector  $[u_{ai,\mathcal{L}} \ v_{ai,\mathcal{L}} \ w_{ai,\mathcal{L}}]^T$  is an evaluation of the wind field at

$$\begin{bmatrix} x_{ai,\mathcal{L}} \\ y_{ai,\mathcal{L}} \\ z_{ai,\mathcal{L}} \end{bmatrix} = \begin{bmatrix} x_{i,\mathcal{L}} \\ y_{i,\mathcal{L}} \\ z_{i,\mathcal{L}} \end{bmatrix} + a \begin{bmatrix} x_{ni,\mathcal{L}} \\ y_{ni,\mathcal{L}} \\ z_{ni,\mathcal{L}} \end{bmatrix}. \quad (2.11)$$

The range weighting function for the pulsed lidar system considered in this work is approximated by a Gaussian function (see Figure 2). Following [CARIOU \(2013\)](#), the function is parameterized by a standard deviation  $\sigma_L$  depending on the Full Width at Half Maximum (FWHM)

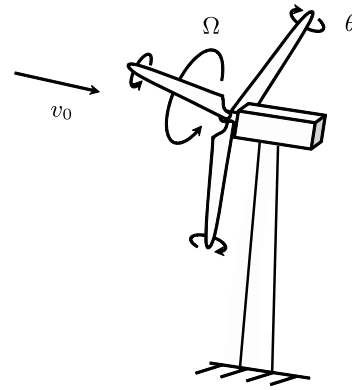


**Figure 3:** Reduced nonlinear wind turbine model with rotor speed  $\Omega$ , collective pitch angle  $\theta$  and rotor effective wind speed  $v_0$ .

of  $W_L = 30$  m:

$$f_{rw}(a) = \frac{1}{\sigma_L \sqrt{2\pi}} \exp\left(-\frac{a^2}{2\sigma_L^2}\right)$$

with  $\sigma_L = \frac{W_L}{2\sqrt{2 \ln 2}}$ . (2.12)

### 2.3 Wind turbine modeling

A simplified wind turbine model as illustrated in Figure 3 is used in this work to calculate the rotor effective wind speed  $v_0$  from turbine data.

The turbine is modeled with the rotor angular speed  $\Omega$  as the only Degree of Freedom (DOF):

$$J\dot{\Omega} = M_a - M_{LSS}. \quad (2.13)$$

Here,  $J$  is the sum of the moments of inertia around the rotation axis. The low speed shaft torque  $M_{LSS}$  is

$$M_{LSS} = \frac{P_{el}}{\eta_{el}\Omega}, \quad (2.14)$$

where  $P_{el}$  is the electrical power and  $\eta_{el}$  is the efficiency of the electro-mechanical energy conversion. The aerodynamic torque acting on the rotor with radius  $R$  is

$$M_a = \frac{1}{2} \rho \pi R^3 \frac{c_P(\lambda, \theta)}{\lambda} v_0^2, \quad (2.15)$$

where  $\rho$  is the air density,  $\theta$  the collective pitch angle, and  $\lambda$  the tip-speed ratio, defined as

$$\lambda = \frac{\Omega R}{v_0}, \quad (2.16)$$

and  $c_P$  is the effective power coefficient. A two dimensional look-up table for  $c_P(\lambda, \theta)$  is obtained from steady state simulations with a full aero-elastic simulation model.



**Figure 4:** Test site close to Grevesmühlen: KENERSYS K110 wind turbine (right) with meteorological mast (left).

**Table 1:** Basic specifications of the KENERSYS K110 turbine<sup>1</sup>.

Rotor diameter	$D$	109	m
Hub height	$z_H$	95	m
Rated power output	$P_{\text{rated}}$	2.4	MW
Rated rotor speed	$\Omega_{\text{rated}}$	12.8	rpm
Rated wind speed	$v_{\text{rated}}$	10.2	m/s
Cutout wind speed	$v_{\text{cutout}}$	20.0	m/s
Turbine and turbulence class	–	III A	

### 3 Test Environment

In this section the test site, wind turbine and lidar system for the experiment are briefly described.

#### 3.1 Test site Grevesmühlen

The experiment is performed at the KENERSYS wind turbine test site, see Figure 4. The site is located in the North-East of Germany, approximately 20 km south of the Baltic Sea and close to the town Grevesmühlen. The terrain at the test site is essentially flat and dominated by farmland with hedges and few large trees. Some forest areas exist as well, but are all situated more than 1 km away from the turbine. The meteorological mast is located 295 m south-west (210 deg) of the turbine and provides a long record of environmental measurements. At wind speeds above 10 m/s the turbulence intensity is mostly in the range of 12 to 16 % for the relevant sectors. The power law wind shear exponent is mostly in the range of 0.2 to 0.3.

#### 3.2 KENERSYS K110 wind turbine

The KENERSYS K110 is a state-of-the-art variable-speed, pitch-controlled wind turbine. It is designed especially for low wind regimes. With a rotor diameter of 109 m and a rated power output of 2.4 MW it yields a relatively low rating of 255 W/m<sup>2</sup>. The main turbine parameters can be found in Table 1. In this experiment, the operating wind turbine is used to align the lidar measurements with the mean wind direction and to provide a reference signal for the rotor effective wind speed.



**Figure 5:** Scanning lidar system installed on the nacelle of the KENERSYS K110.

#### 3.3 SWE scanning lidar system

A scanning lidar system was installed on the K110 in early 2013. It was placed on a rack which was mounted horizontally on the nacelle, as can be seen in Figure 5.

The system consists of two parts: a Windcube V1 from Leosphere<sup>2</sup> and a scanner unit developed at the University of Stuttgart. Since the original Windcube was designed for site assessment with its beam pointing upwards, a two DOF mirror for redirecting the beam was installed in a second casing, which the beam to point sideways. Modified software synchronizes the laser with the two motor stages. Within mechanical constraints, this software allows a free design of the scanning trajectories with 1 to 50 points. The accessible area is a  $0.75D \times 0.75D$  square or a circle with a radius of  $0.5D$  at  $1D$  distance. The modified software allows the use of up to 5 range gates. The minimum range gate is at a distance of 40 m and the maximum range is around 200 m depending on the aerosol concentration. See (RETTENMEIER et al., 2013) for more details.

### 4 Wind evolution detection

With the exponential wind evolution model (2.6), the detection of the wind evolution can be broken down to identify the longitudinal decay parameter  $\alpha$ . The difficulties in detecting  $\alpha$  directly in a real experiment are described in this section. The exponential wind evolution

<sup>1</sup>[www.kenersys.com/K110-2-4MW.46.0.html](http://www.kenersys.com/K110-2-4MW.46.0.html)

<sup>2</sup>[www.leosphere.com](http://www.leosphere.com)

**Table 2:** Measurement positions in the lidar coordinate system.

range gate $i$	$x_{i,\mathcal{L}}$ [D]	$y_{i,\mathcal{L}}$ [D]	$z_{i,\mathcal{L}}$ [D]
1 •	0.50	0	0
2 •	0.75	0	0
3 •	1.00	0	0
4 •	1.25	0	0
5 •	1.50	0	0

is incorporated into a model of the coherence between lidar measurements and considers the impact of yaw misalignment, limitation to line-of-sight wind speed, and volume measurement. Finally, the longitudinal decay parameter is indirectly identified by fitting the measured coherence to the modeled one.

### 4.1 Experimental setup

For the detection of the wind evolution, the motion of the mirrors of the scanning lidar has been set to zero and the 5 range gates have been fixed, see Table 2. Each measurement acquisition is averaged over 12000 pulses corresponding to an acquisition time of  $T_{ACQ} = 1$  s. The maximum blocking time of the rotating blades has been identified to 0.5 s. Thus, the high acquisition time has been chosen to guaranty a minimum of 6000 pulses within one measurement to obtain sufficient backscatter for all range gates. This trajectory was applied during 14 days in December 2013. The data is split into 10-minute-blocks and 80 blocks are selected for the analysis in this section according to the following aspects:

- The lidar availability is 100 % at all distances. Availability of 100 % for the given system is defined by the Carrier-to-Noise-Ratio (CNR) being over  $-22$  dB.
- Mean wind speed measured by the sonic on the meteorological mast  $\bar{u}_{S,\mathcal{W}}$  is over 10 m/s. This value is chosen, because the wind evolution is detected to optimize the lidar scan pattern for collective pitch feed-forward control, which is enabled above 10 m/s.
- The averaged wind direction measured by a sonic anemometer on the meteorological mast at hub height is within a  $\pm 30$  deg sector from the direction towards the turbine (210 deg). This value is chosen to provide a reliable measurement of the yaw misalignment.

The measurements are collected from an operating turbine, which controls its yaw angle to face the actual wind direction based on a wind vane installed on the nacelle. However, common yaw controllers only react, if the absolute yaw misalignment  $\alpha_H$  averaged over 10 minutes is exceeding 10 deg (HAU, 2006). Thus, the longitudinal decay  $\gamma_{ij,ux}^2$  can only be detected with the chosen setup as a part of the combined longitudinal and lateral decay, see Figure 6. Additionally, the used lidar system is only able to measure the line-of-sight wind speed within a probe volume. Thus, the coherence model is successively extended in the following three subsections to account for these effects.

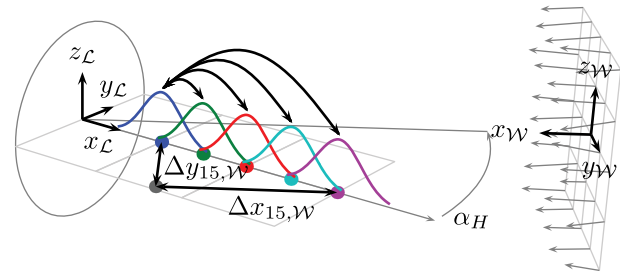


**Figure 6:** Realistic case of wind evolution detection.

### 4.2 Impact of yaw misalignment

Following SCHLIPF et al. (2013a) and LAKS et al. (2013), it is assumed that the coherence of the longitudinal wind component between the points  $i$  and  $j$  with the longitudinal separation  $\Delta x_{ij,\mathcal{W}}$  and the lateral separation  $\Delta y_{ij,\mathcal{W}}$  is a product of the longitudinal (2.6) and the lateral decay (2.5):

$$\gamma_{ij,u}^2 = \gamma_{ij,ux}^2 \gamma_{ij,uy}^2$$

with  $\gamma_{ij,uy}^2 = \exp(-2\kappa \Delta y_{ij,\mathcal{W}})$ . (4.1)

Since the yaw misalignment  $\alpha_H$  is measurable, using a method which will be explained in Section 4.6, the longitudinal separation  $\Delta x_{ij,\mathcal{W}}$  and the lateral separation  $\Delta y_{ij,\mathcal{W}}$  can be obtained by

$$\begin{aligned} \Delta x_{ij,\mathcal{W}} &= |\cos(\alpha_H) \Delta x_{ij,\mathcal{L}}| \\ \Delta y_{ij,\mathcal{W}} &= |\sin(\alpha_H) \Delta x_{ij,\mathcal{L}}|. \end{aligned} \quad (4.2)$$

### 4.3 Impact of line-of-sight measurements

However, due to the limitation to line-of-sight measurements, the coherence of the longitudinal wind component  $\gamma_{ij,u}^2$  cannot be identified directly. The approach presented in (SCHLIPF et al., 2013a) can be used to model the coherence  $\gamma_{ij,losP}$  between the line-of-sight measurements (2.7) in two points  $i$  and  $j$ . The impact of the probe volume is added in Section 4.4. The basic idea is summarized in the following steps:

1. Define the equation of the measurement signal as a sum of wind velocity component signals.
2. Define its representation in the Fourier domain.
3. Combine the parts of the Fourier transform to fore-known spectra of wind components and calculate the auto- and cross-spectra of the signals.
4. Calculate the coherence between the signals based on its definition from the auto- and cross-spectra.

For the first step, the line-of-sight wind speeds are simplified by using the lidar point-measurement model (2.7), the normalized laser vector (2.8), the coordinates from Table 2, and the coordinate transformation (2.9):

$$v_{losP,i} = \cos(\alpha_H)u_{i,\mathcal{W}} - \sin(\alpha_H)v_{i,\mathcal{W}}. \quad (4.3)$$

The wind velocity components need to be set in the wind coordinate system, where the spectra are defined.

In the second step, the signals of the line-of-sight wind speeds are transformed using the property of linearity of the Fourier transform:

$$\mathcal{F}\{v_{losP,i}\} = \cos(\alpha_H)\mathcal{F}\{u_{i,\mathcal{W}}\} - \sin(\alpha_H)\mathcal{F}\{v_{i,\mathcal{W}}\}. \quad (4.4)$$

In the third step, the auto-spectrum  $S_{ii,losP}$  of each signal  $v_{losP,i}$  and the cross-spectrum  $S_{ij,losP}$  between a signal  $v_{losP,i}$  and a signal  $v_{losP,j}$  are calculated. Here, the auto- and cross-spectra of signals are defined as the product of the corresponding Fourier transform  $\mathcal{F}\{\}$  and its complex conjugate  $\mathcal{F}^*\{\}$  following the definition by BENDAT and PIERSOL (2012). All mean operators and scaling constants are omitted, since the Fourier transforms are replaced at the end by known auto- and cross-spectra and all scaling constants can be canceled out. In the Kaimal model no correlation between the longitudinal and the lateral wind velocity component is defined. This simplifies the calculation of the auto-spectrum  $S$  of each line-of-sight point measurement to

$$\begin{aligned} S_{ii,losP} &= \mathcal{F}\{v_{losP,i}\}\mathcal{F}^*\{v_{losP,i}\} \\ &= \cos^2(\alpha_H)S_{ii,u} + \sin^2(\alpha_H)S_{ii,v}. \end{aligned} \quad (4.5)$$

Further, the cross-spectrum  $S_{ij,u}$  of the longitudinal wind velocity component between two points  $i$  and  $j$  is calculated using the definition of the coherence (2.4) for the combined longitudinal and lateral decay (4.1):

$$\gamma_{ij,u}^2 = \frac{|S_{ij,u}|^2}{S_{ii,u}S_{jj,u}} \Rightarrow S_{ij,u} = \gamma_{ij,u}S_{ii,u}. \quad (4.6)$$

Here, the auto-spectra of the longitudinal wind velocity component in points  $i$  and  $j$  are equal ( $S_{ii,u} = S_{jj,u}$ ). Also, there is no phase shift between the longitudinal wind speed component in point  $i$  and  $j$ , if the signals are shifted in time accordingly ( $|S_{ij,u}| = S_{ij,u}$ ).

With Equation (4.6) and the impact of the yaw misalignment (4.1), the cross-spectrum  $S_{ij,losP}$  of line-of-sight point measurements between point  $i$  and  $j \neq i$  is

$$\begin{aligned} S_{ij,losP} &= \mathcal{F}\{v_{losP,i}\}\mathcal{F}^*\{v_{losP,j}\} = \cos^2(\alpha_H)S_{ij,u} \\ &= \cos^2(\alpha_H)\gamma_{ij,ux}\gamma_{ij,uy}S_{ii,u}. \end{aligned} \quad (4.7)$$

In the fourth step, the coherence  $\gamma_{ij,losP}^2$  between the line-of-sight measurements in point  $i$  and  $j$  can be calculated based on its definition and considerations similar to the ones discussed for Equation (4.6):

$$\begin{aligned} \gamma_{ij,losP} &= \sqrt{\frac{|S_{ij,losP}|^2}{S_{ii,losP}S_{jj,losP}}} = \frac{S_{ij,losP}}{S_{ii,losP}} \\ &= \frac{\cos^2(\alpha_H)\gamma_{ij,ux}\gamma_{ij,uy}S_{ii,u}}{\cos^2(\alpha_H)S_{ii,u} + \sin^2(\alpha_H)S_{ii,v}}. \end{aligned} \quad (4.8)$$

This detailed calculation shows, that  $\gamma_{ij,losP}$  can be expressed only by known spectral properties from the Kaimal model and the exponential wind evolution model. However, further extension of the model is necessary to additionally include the effect of the pulse volume of the lidar measurements.

#### 4.4 Impact of volume measurements

Similar to the simplification made to the lidar point measurement in Equation (4.3), the equation of the lidar volume measurement (2.10) can be approximated with a Riemann sum over  $n_w$  weights to

$$v_{losV,i} \approx \sum_{w=1}^{n_w} f_{rw,w}(\cos(\alpha_H)u_{wi,\mathcal{W}} - \sin(\alpha_H)v_{wi,\mathcal{W}}), \quad (4.9)$$

where the weight  $f_{rw,w}$  is the range weighting function  $f_{rw}$  defined in (2.12) at the distance  $a_w$  from the point  $i$ , normalized by the sum of all weights:

$$f_{rw,w} = \frac{f_{rw}(a_w)}{\sum_{w=1}^{n_w} f_{rw}(a_w)}. \quad (4.10)$$

The used discrete distances  $a_w$  are displayed in Figure 2. Similar to (2.11),  $u_{wi,\mathcal{W}}$  and  $v_{wi,\mathcal{W}}$  are the longitudinal and lateral wind velocity components at the distance  $a_w$  from point  $i$ , respectively.

Based on Equation (4.9), the second to the fourth step of Section 4.3 are applied to obtain the coherence  $\gamma_{ij,losV}$  between line-of-sight volume measurements in point  $i$  and  $j$ . The equation becomes too complex to be displayed in detail, since the differences in the longitudinal and lateral separation vary for the combinations of the discretized pulse volumes and since the convolution of the weighting function needs to be considered.

Figure 7 shows the exponential wind evolution model for a distance of  $\Delta x_{12,\mathcal{W}} = 0.25D = 27.25$  m and a longitudinal decay parameter of  $\alpha = 0.4$  as roughly estimated in (SCHLIPF and CHENG, 2013). The pure wind evolution model is then extended successively. When considering a yaw misalignment of  $\alpha_H = 3$  deg, the coherence drops due to the additional lateral decay. The impact of the additional line-of-sight point measurement is minor due to the relatively small yaw misalignment. When additionally the range weighting function  $f_{rw}$  with a FWHM of 30 m is considered, the coherence changes its shape due to the overlapping volumes as illustrated in Figure 6. The coherences are plotted over the wavenumber  $k$ , because the Kaimal turbulence model and thus all modeled coherences can be calculated independent from the mean wind speed by replacing the frequency  $f$  with

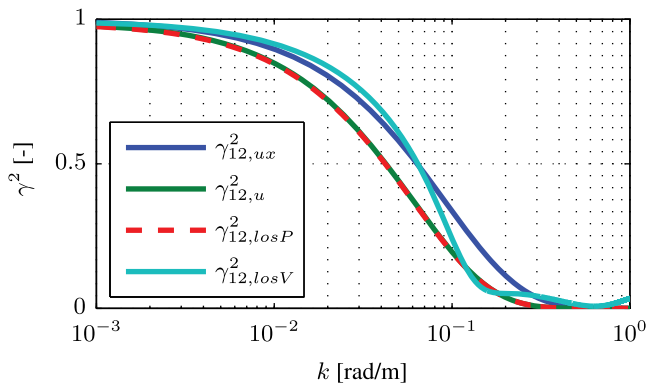


**Figure 7:** Impact of yaw misalignment ( $\gamma_{12,u}^2$ ), line-of-sight ( $\gamma_{12,losP}^2$ ) and volume measurement ( $\gamma_{12,losV}^2$ ) to the wind evolution model ( $\gamma_{12,ux}^2$ ).

the wavenumber  $k = 2\pi f/\bar{u}$ . The used coherence models are also independent of the turbulence intensity, since all three Kaimal auto-spectra are proportional to the variance  $\sigma_u^2$ , which is canceled out when calculating the coherence. However, more detailed wind evolution models might depend on the turbulence or other parameters.

### 4.5 Impact of time averaging

The used lidar system averages Doppler spectra over  $T_{ACQ} = 1$  s to determine the Doppler frequency shift. The effective averaging time varies due to the blockage of the rotating blades. If this effect is neglected, the time averaged lidar volume measurement can be modeled by a running average over the lidar volume measurement:

$$v_{los,i} = v_{losV,i} * \text{rect}\left(\frac{t - \frac{T_{ACQ}}{2}}{T_{ACQ}}\right), \quad (4.11)$$

where  $\text{rect}()$  is the rectangular function and  $*$  denotes convolution, which is translated by the Fourier transformation to a multiplication of the individual Fourier transforms. Therefore, the resulting auto-spectrum is

$$\begin{aligned} S_{\ddot{u},los} &= \mathcal{F}\{v_{los,i}\}\mathcal{F}^*\{v_{los,i}\} \\ &= \text{sinc}^2(fT_{ACQ})S_{\ddot{u},losV}, \end{aligned} \quad (4.12)$$

where  $\text{sinc}()$  is the normalized cardinal sine function used in signal processing.

Since all signals are averaged over the same time  $T_{ACQ}$ , all auto- and cross-spectra will be multiplied with  $\text{sinc}^2(fT_{ACQ})$ . This factor will be finally canceled out, when calculating the coherence  $\gamma_{ij,los}^2$  between the time-averaged line-of-sight volume measurements in points  $i$  and  $j$ . Therefore, it is not necessary to consider the time average when detecting the coherence and thus  $\gamma_{ij,los}^2$  is equal to the coherence  $\gamma_{ij,losV}^2$  from Section 4.4 without the time average.

Eventually, the coherence model with incorporated wind evolution is set up. However, it is necessary to determine the yaw misalignment (Section 4.6) before the wind evolution can be identified (Section 4.7).

### 4.6 Detection of the yaw misalignment

Obtaining an accurate measurement of the yaw misalignment is a challenging task. The wind vane installed on the nacelle of wind turbines is in general disturbed by the local flow around the nacelle and blades. A more precise method can be using the difference between the yaw position and the wind direction measured by the sonic anemometer on the meteorological mast. However, there are several sources of errors:

- an offset in the yaw position sensor of the nacelle
- an offset in the installation angle of the sonic anemometer on the meteorological mast
- an offset in the installation angle of the lidar system on the nacelle
- change of the wind direction from the meteorological mast to the turbine

The offset between the nacelle position and the lidar installation might be found by using a range gate close to the mast (here 295 m). The turbine could then be yawed or the lidar could perform a horizontal scan. The position of the mast should then be detected by the high reflection and a peak in the Doppler spectra at 0 m/s. However, this procedure cannot account for the change in the wind direction or the offset of the sonic anemometer.

To overcome this problem, the following procedure is applied to the 10-minute-blocks selected in Section 4.1 to detect the bias  $\alpha_{H,0}$  of the yaw misalignment for each nacelle yaw position.

1. The correlation coefficient  $\rho_{15,los}$  (peak of the normalized cross correlation) between the line-of-sight wind speed from the first and the last distance is determined for each 10-minutes-block.
2. The biased yaw misalignment  $\alpha_{H,b}$  is calculated for each block as the difference between the nacelle yaw position and the wind direction measured by the sonic anemometer on the meteorological mast.
3. For each yaw position the blocks within  $\pm 10$  deg are selected and the correlation coefficients are fitted by heuristically assuming a linear decay. For this purpose, the following minimization problem is solved:

$$\min_{a,b,\alpha_{H,0}} \left\| \rho_{15,los} - (a|\alpha_{H,b} - \alpha_{H,0}| + b) \right\|_2. \quad (4.13)$$

4. The corrected yaw misalignment is then

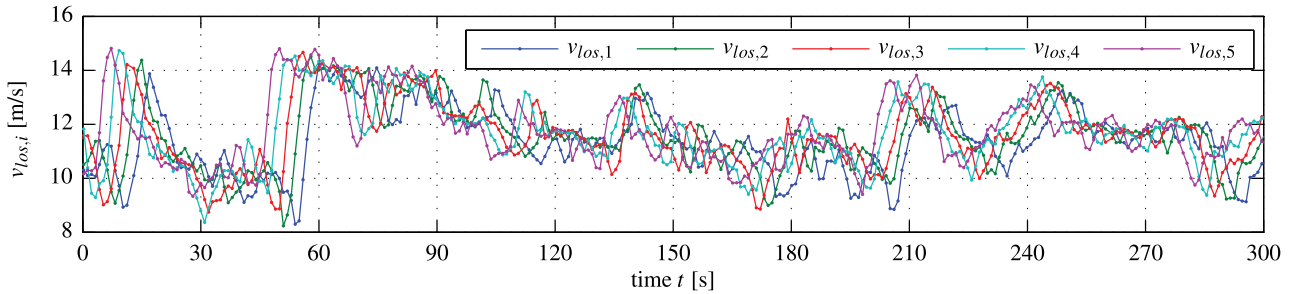
$$\alpha_H = \alpha_{H,b} - \alpha_{H,0}. \quad (4.14)$$

### 4.7 Identification of the Wind Evolution

The longitudinal decay parameter is finally evaluated by comparing the estimated coherence from the measurements to the coherence of the exponential evolution

**Table 3:** Overview of evaluated 1-hour-blocks from the 5<sup>th</sup> of December 2013.

Block ID	Start time	mean wind speed $\bar{u}_{s,w}$ [m/s]	mean turbulence intensity [-]	nacelle yaw position [deg]	mean yaw misalignment $\alpha_H$ [deg]	standard deviation yaw misalignment [deg]	longitudinal decay parameter $\alpha$ [-]
1	07:00	11.2	12.1	226	0.8	5.21	0.187
2	08:00	12.0	13.4	226	-0.8	6.23	0.210
3	09:00	13.1	14.3	226	2.9	6.49	0.179
4	11:00	15.9	14.5	219	2.1	6.76	0.261

**Figure 8:** Example of staring lidar measurements at all five distances (5 min excerpt from block 1): While the signals are similar at low frequencies, differences in high frequencies are visible.

model extended by the model for yaw misalignment and lidar volume filtering.

The process of estimating the coherence from time signals is quite complex and the quality of the results expressed for example by the bias and random error depends on several parameters (CARTER et al., 1973). In this paper, Welch's averaged periodogram method is used, where basically the signals are divided into several sections. The spectra are then calculated by a FFT for each section and averaged over all sections. By dividing the signals of the 10-minute-blocks in more sections, the bias and the random error can be decreased. However, there will be fewer data points per block and thereby the frequency resolution will degrade. Therefore, the data base is screened for continuous 1-hour-blocks and 4 blocks in the morning on the 5<sup>th</sup> of December 2013 are selected. Details such as mean wind speed or turbulence intensity can be found in Table 3. Figure 8 shows an example of the line-of-sight wind speeds of block 1 (5 min of data).

The coherences between the line-of-sight wind speeds for each individual 1-hour-block are estimated by the following procedure:

1. The delay of the signals is determined by the peak of the cross correlation to the first distance.
2. The signals are time shifted with the delays determined in the first step, such that all signals are in phase.
3. The coherences are estimated using Welch's averaged periodogram method<sup>3</sup>.

The estimated coherences  $\hat{\gamma}_{1j}^2$  for each 1-hour-block are plotted in Figure 9 (solid lines). The coherences in blocks 1 and 2 are similar due to comparable absolute yaw misalignment, but differ from blocks 3 and 4 with higher yaw misalignment.

The longitudinal decay parameter for each data block is eventually found by fitting the modeled coherences  $\gamma_{1j}^2$  to the estimated coherences  $\hat{\gamma}_{1j}^2$ . This is done by the following iterative procedure:

1. The coherence bandwidth  $\hat{k}_{0.5,1j}$ , where the coherences reach the value of 0.5, is determined for each estimated coherence  $\hat{\gamma}_{1j}^2$ . This value is chosen as a compromise between computational effort and robustness.
2. The coherences  $\gamma_{1j}^2$  are calculated with the corrected yaw misalignment  $\alpha_H$  from Table 3 and an initial longitudinal decay parameter  $\alpha$ .
3. The coherence bandwidth  $k_{0.5,1j}$  from each modeled coherence  $\gamma_{1j}^2$  is determined.
4. The second and third step are repeated with an updated longitudinal decay parameter  $\alpha$  solving the following minimization problem:

$$\min_{\alpha} \sum_{j=2}^5 (\hat{k}_{0.5,j} - k_{0.5,j})^2. \quad (4.15)$$

The fitted coherences are added to Figure 9. The shape of the modeled coherences corresponds well to the estimated coherences from the data. This agreement justifies the extension of the wind evolution model by the effects of the yaw misalignment, line-of-sight limitation and volume measurement (comparison see Figure 7).

<sup>3</sup>Done with mscohere of The MathWorks Inc., Matlab R2013b, Natick, USA (2013), using 32 data sections, 50% overlap, and a cosine windows (Hamming) to decrease the spectral leakage.

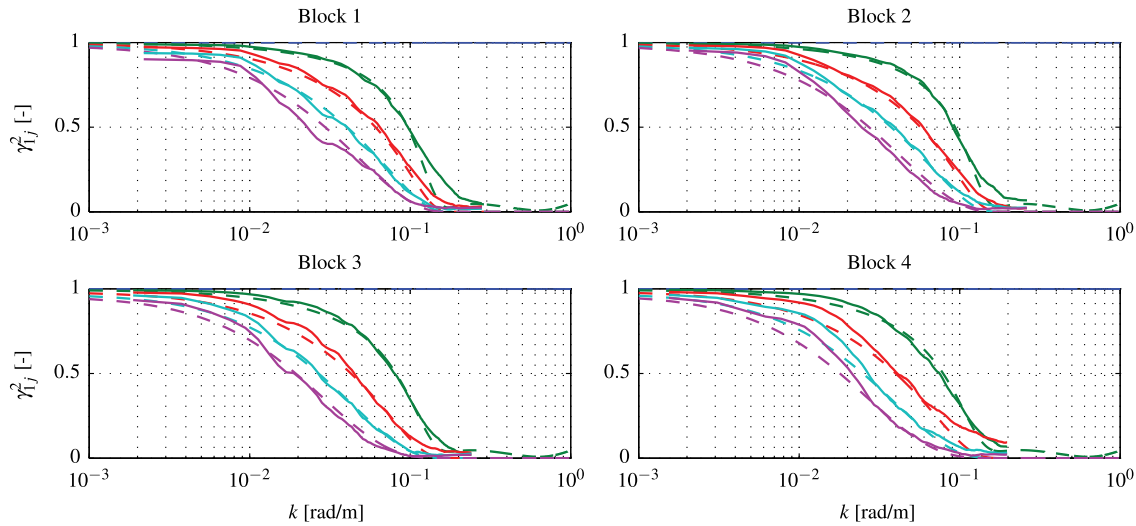


**Figure 9:** Estimated coherences between the line-of-sight measurements from all five distances (for colors and details see Table 2) and the line-of-sight measurement of the first distance (solid). Modeled coherences with integrated fitted longitudinal decay parameter (dashed).

Finally, the detected longitudinal decay parameters can be found in Table 3 and cover a range from 0.179 to 0.261. Further work is necessary to provide a more accurate wind evolution model. However, for field testing of lidar-assisted collective pitch control this very rough estimate already provides valuable information to adjust the scan trajectory.

In the optimization of the scan trajectory presented in the next section, the longitudinal decay parameter is set to the average value of 0.2.

## 5 Trajectory optimization

For lidar systems used for control it is crucial to provide a signal of the rotor effective wind, which is on the one hand sufficiently correlated to the wind speed affecting the turbine to improve the control performance. On the other hand, the signals must be provided with enough preview to filter out the uncorrelated frequencies which will cause unnecessary control action, inducing undesired loads. However, there are several interacting effects which determine how well the wind speed is predicted. The approach presented in (SCHLIPF et al., 2013a) models the correlation between lidar systems and wind turbines using Kaimal wind spectra. The derived model accounts for different measurement configurations and spatial averaging of the lidar system, different rotor sizes and wind evolution. The wind evolution is parameterized with the longitudinal decay parameter identified in the previous section.

In beginning of this section, the basic idea of the approach is explained. Then the approach is used to optimize the SWE lidar system for the K110 wind turbine. The outcome is on the one hand a scanning pattern, which provides a signal of the rotor effective wind speed for collective pitch feedforward control with the best possible correlation to the wind sensed by the turbine and with sufficient preview to filter out uncorrelated

frequencies. On the other hand, the approach provides a transfer function, which is used to determine the optimal filter for the feedforward controller. The optimized scanning pattern has been applied in the experiment. At the end of this section, the correlation of the turbine’s reaction to the signal from the lidar system is presented.

### 5.1 Motivation for the correlation model

The correlation between lidar systems and wind turbines is expressed by the magnitude squared coherence  $\gamma_{RL}^2$  between the rotor effective wind speed measured by the lidar and sensed by the turbine’s rotor, defined as

$$\gamma_{RL}^2 = \frac{|S_{RL}|^2}{S_{RR}S_{LL}}, \quad (5.1)$$

where  $S_{RL}$ ,  $S_{RR}$ , and  $S_{LL}$  are the cross-spectrum between both signals and the auto-spectra of the signals from the turbine and the lidar, respectively. Furthermore, it is important to calculate the transfer function from the lidar signal to the rotor signal. Although nothing is “transferred” in a classical sense, the transfer function between two signals is defined according to BENDAT and PIERSOL (2012) by

$$G_{RL} = \frac{S_{RL}}{S_{LL}}. \quad (5.2)$$

Based on this transfer function, an adaptive filter can be designed to filter out all uncorrelated frequencies avoiding wrong and harmful control action, see SCHLIPF and CHENG (2013) and SIMLEY and PAO (2013b).

In order to determine the correlation between lidar measurements and turbine reaction, the cross- and auto-spectra can be estimated by a simulation study in the time domain, see Figure 10. Therefore, the wind components  $u_W, v_W, w_W$  have to be generated using a discrete inverse Fourier transformation (iFFT) based on wind spectra and a wind evolution model. Then, the wind

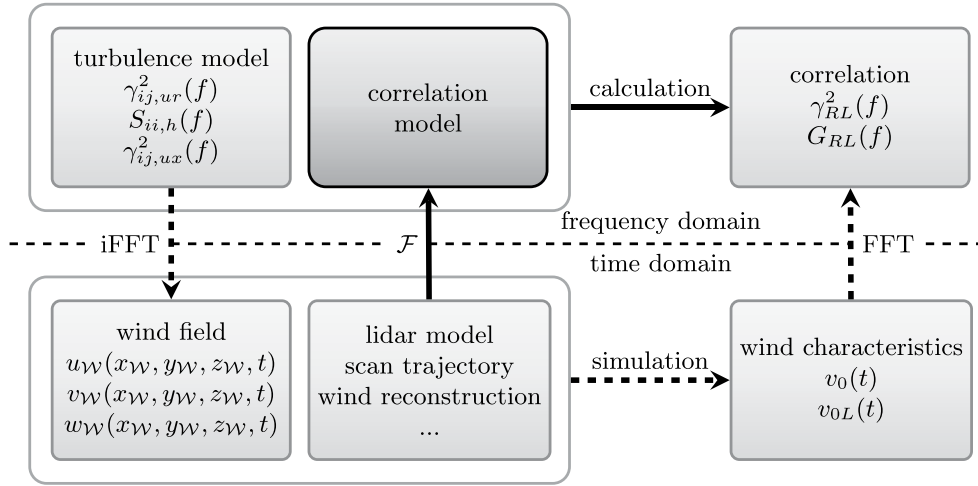


**Figure 10:** Basic idea of the correlation model: The correlation between a lidar system and a turbine’s reaction is directly calculated in the frequency domain with the Fourier transform of equations for the simulation and the turbulence model (solid) – instead of generating a wind field, performing time domain simulations and estimating the correlation (dashed).

fields have to be scanned by a lidar simulator to obtain the line of sight wind speeds. In a next step, the rotor effective wind speed  $v_0$  and its lidar estimate  $v_{0L}$  need to be determined from the simulation data. In the last step, the auto- and cross-spectra can be estimated with a FFT and the estimate of the coherence  $\gamma_{RL}^2$  and the transfer function  $G_{RL}$  are determined by (5.1) and (5.2). Finally, the quality of the time consuming estimation depends and the length of the simulation.

In order to avoid this issue, the method proposed in (SCHLIPF et al., 2013a) calculates the cross- and auto-spectra directly from the wind turbulence and evolution model and the Fourier transform of the measurement equations and reconstruction method, see Figure 10. However, a purely analytic model is only achieved for a basic setup. Therefore, partial discretization is also necessary to model more realistic setups.

Similar to the calculation of the auto- and cross-spectra of the line-of-sight measurements in Equations (4.5) and (4.7), the auto-spectra of the rotor effective wind speed  $v_0$  and its lidar estimate  $v_{0L}$  as well as the cross-spectrum between the two signals is defined – omitting all scaling constants and mean operators – by

$$\begin{aligned} S_{RR} &= \mathcal{F}\{v_0\}\mathcal{F}^*\{v_0\} \\ S_{LL} &= \mathcal{F}\{v_{0L}\}\mathcal{F}^*\{v_{0L}\} \\ S_{RL} &= \mathcal{F}\{v_0\}\mathcal{F}^*\{v_{0L}\}. \end{aligned} \quad (5.3)$$

The auto- and cross-spectra are derived in the following subsection.

## 5.2 Calculation of auto- and cross-spectra

When assuming perfect alignment ( $\alpha_H = 0$  deg), the rotor effective wind speed  $v_0$  of a turbine can be modeled as the mean of  $n$  longitudinal wind components evenly spaced across the rotor disk:

$$v_0 = \frac{1}{n} \sum_{i=1}^n u_{i,\mathcal{W}}. \quad (5.4)$$

With Equation (5.3) and (5.4) and by replacing the cross-spectra  $S_{ij,u}$  by  $\gamma_{ij,ur} S_{ii,u}$  based on the considerations in (4.6), the rotor effective spectrum is expressed by a sum of coherence functions and auto-spectra:

$$S_{RR} = \frac{S_{ii,u}}{n^2} \sum_{i=1}^n \sum_{j=1}^n \gamma_{ij,ur}. \quad (5.5)$$

In order to calculate the auto-spectrum  $S_{LL}$  of the lidar estimate of the rotor effective wind speed, the four steps presented in Section 4.3 are applied. In the first step the signal of the rotor effective wind speed estimate needs to be defined as a sum of wind velocity components.

For this purpose, the rotor effective wind speed estimate is calculated from corrected line-of-sight wind speeds using the equation of the dynamic wind field reconstruction (see (SCHLIPF et al., 2014) for more details). The approach is independent of the scan pattern and the number of measurement distances. However, it is beneficial, if the measurements are evenly distributed over the rotor disc. This can be achieved by circular scans. The dynamic wind field reconstruction applied in the field testing assumes perfect alignment and lidar point measurements (2.7) and the estimated longitudinal wind speed component in each measurement point is

$$\hat{u}_{i,\mathcal{W}} = \frac{v_{los,i}}{x_{ni,\mathcal{W}}}, \quad (5.6)$$

where  $x_{ni,\mathcal{W}}$  is obtained by transforming the normalized laser vector (2.8) into the wind coordinate system  $\mathcal{W}$ . For each distance  $j$ , the estimated longitudinal wind speeds are averaged after every new measurement over the last full trajectory of  $n_p$  data points:

$$v_{0Lj} = \frac{1}{n_p} \sum_{i=1}^{n_p} \hat{u}_{i,\mathcal{W}}. \quad (5.7)$$

The obtained time series  $v_{0Lj}$  from  $n_d$  distances are

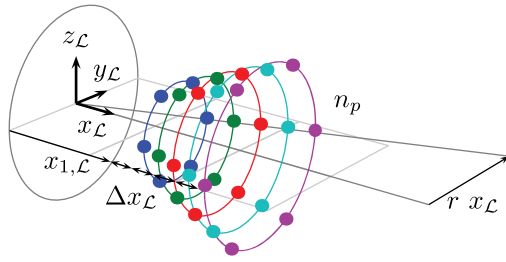


**Figure 11:** Variables for the trajectory optimization.

shifted by the times

$$T_{\text{Taylor},ij} = \frac{\Delta x_{ij,W}}{\bar{u}}. \quad (5.8)$$

according to Taylor’s frozen turbulence hypothesis and combined to form the rotor effective wind speed  $v_{0L}$ :

$$v_{0L}(t) = \frac{1}{n_d} \sum_{j=1}^{n_d} v_{0Lj}(t - T_{\text{Taylor},1j}). \quad (5.9)$$

Similar to Equation (4.9),  $v_{los,i}$  is replaced by the discrete form of (2.10):

$$v_{los,i} = \sum_{w=1}^{n_w} f_{rw,w}(x_{ni,W} u_{i,W} + y_{ni,W} v_{i,W} + z_{ni,W} w_{i,W}). \quad (5.10)$$

Combining Equation (5.6) to (5.10),  $v_{0L}$  can be expressed by a pure sum of wind velocity components. Therefore, the second to the fourth step of Section 4.3 can be applied straightforwardly to determine the auto-spectra  $S_{LL}$ . With the Fourier transforms of  $v_0$  and  $v_{0L}$ , the cross-spectrum  $S_{RL}$  can be determined. Since the signals are shifted with (5.9) to the rotor, almost all components are in phase. Only the volume weighting introduces complex parts into  $S_{LL}$  and  $S_{RL}$ , but are canceled out due to the symmetry of the used weighting function (2.12). Similar to the rotor average, simultaneous measurement at all points is assumed.

With this method, the auto- and cross-spectra can be calculated in an automated way for different rotor and lidar system setups.

### 5.3 Constrained optimization problem

An optimization problem consists typically of a cost function (what should be optimized), optimization variables (which parameter can be changed), and constraints (which conditions have to be fulfilled).

In the case of finding an optimal configuration for a lidar system, the cost function depends on the application. In the present field testing campaign the lidar system should provide a signal of the rotor effective wind speed for collective pitch feedforward control, which is correlated to the rotor effective wind speed felt by the turbine in an optimal sense. If the lidar is additionally used for individual pitch control or for yaw control,

other trajectories will be better suited (SIMLEY and PAO, 2013b; RAACH et al., 2014).

There are several possibilities for how to define the “optimal sense”. Measures in the time domain such as the mean square error proposed by SIMLEY and PAO (2013b) or the correlation coefficient are very useful measures under simulation conditions. Those measures are also simple to determine from field testing data. However, they sum up effects over all frequencies. This is problematic, because real signals of the rotor effective wind speed estimated from turbine or lidar data often differ from simulated ones in the way that they include noise from the measurements or the lidar movements. Thus, frequency-based measures have the advantage for the comparison to real data that one can focus on the relevant frequency domain. Unfavorably frequency-based measures are more difficult to determine. In (SCHLIPF et al., 2013a) the maximum coherent wavenumber is proposed, defined by the pole location of a first order low-pass filter whose magnitude best fits the transfer function  $G_{RL}$ . However, less filtering does not automatically lead to better correlation. A better suited measure is the coherence bandwidth as proposed in (DUNNE et al., 2014), which is defined as the wavenumber  $k_{0.5}$ , where the magnitude squared coherence  $\gamma_{RL}^2$  reaches the level of 0.5.

The choice of the optimization variables depends on the flexibility of the lidar system. In the case of the SWE-scanning lidar system, a circular trajectory has been chosen due to simplicity and is parametrized by following variables, see Figure 11:

- $n_p$ : number of points on a circle
- $r$ : radius normalized by its distance from the rotor
- $x_{1,L}$ : position of the first circle
- $\Delta x_L$ : spacing between the circles

The constraints in the present optimization problem can be divided into constraints of the lidar system and in constraints from the applications. The constraints for the SWE-scanning lidar system are:

- Due to mechanical constraints, the normalized radius  $r$  has to be between 0 and 0.5.
- The lidar system is unable to measure at ranges below 40 m. Therefore, for the minimum measurement distance  $x_{1,L}$  has to be larger than  $40 \text{ m} / \sqrt{1 + r^2}$ .
- There is also a limitation of around 200 m for the last range. Therefore, for the last measurement distance  $x_{5,L}$  has to be smaller than  $200 \text{ m} / \sqrt{1 + r^2}$ .

Apart from these lidar system specific constraints, controller specific requirements need to be fulfilled as well. For the collective pitch feedforward controller applied in this campaign, the filtered signal of the rotor effective wind speed has to be transferred to the control system only with a small preview time  $\tau$  before the wind reaches the turbine. Other control strategies such as non-linear model predicted control (SCHLIPF et al., 2013b) can incorporate longer previews. This preview time  $\tau$

is necessary to compensate the pitch actuator dynamics and is typically below 1 s. Therefore, the filtered signal has to be synchronized with the wind reaching the rotor plane with an adaptive buffer time  $T_{\text{buffer}}$ . The corresponding buffer time is obtained from the following considerations: With Taylor's frozen turbulence hypothesis, the wind travels during the time  $T_{\text{Taylor}}$  from the first measurement distance to the turbine. All other measurement distances  $v_{0Lj}$  are shifted to the first one by (5.9). Due to the sequential blockage of the rotating blades, the acquisition time is chosen to  $T_{\text{ACQ}} = 0.8$  s and thus the overall scan time is  $T_{\text{scan}} = n_p T_{\text{ACQ}}$ . By averaging over the full trajectory, all  $v_{0Lj}$  are delayed by  $T_{\text{scan}}/2$ . An additional delay  $T_{\text{filter}}$  is introduced by the filter. Thus, the buffer time is calculated by

$$T_{\text{buffer}} = T_{\text{Taylor}} - \frac{1}{2}T_{\text{scan}} - T_{\text{filter}} - \tau. \quad (5.11)$$

In order to provide the signal in time, the buffer time needs to be non-negative.

As explained in (SCHLIPF et al., 2013a) and (SIMLEY and PAO, 2013b), a filter fitted to the transfer function  $G_{RL}$  is necessary to cancel out all uncorrelated frequencies. Due to its low pass behavior the transfer function is approximated by a first-order filter. This is done by determination of the maximum coherent wavenumber  $\hat{k}$ , where the transfer function reaches a value of  $-23$  dB. The cut-off frequency of the filter is then

$$f_{\text{cutoff}} = \frac{\hat{k}\bar{u}}{2\pi}. \quad (5.12)$$

The first-order filter has a non-linear phase and thus frequency-depending time delays. In previous work (SCHLIPF et al., 2014), the filter delay  $T_{\text{filter}}$  was approximated by the time delay of the first order filter at a relevant frequency.

Here, the overall delay of the filter  $T_{\text{filter}}$  is obtained from the peak of the cross-correlation, which can be calculated for each cutoff frequency  $f_{\text{cutoff}}$  based on the auto-spectrum  $S_{LL}$  from the lidar measurement and the filter transfer function (SCHLIPF, in review).

Thus,  $T_{\text{buffer}}$  can be determined for each setting of the optimization variables and a given mean wind speed  $\bar{u}$ .

Finally, the optimization problem can be formulated:

$$\begin{aligned} & \max_{n_p, r, x_{1,\mathcal{L}}, \Delta x_{\mathcal{L}}} k_{0,5} \\ & \text{such that: } T_{\text{buffer}} \geq 0 \\ & \quad 0.5 \geq r \geq 0 \\ & \quad x_{1,\mathcal{L}} \geq 40 \text{ m} / \sqrt{1+r^2} \\ & \quad x_{5,\mathcal{L}} = x_{1,\mathcal{L}} + 4\Delta x_{\mathcal{L}} \geq 200 \text{ m} / \sqrt{1+r^2}. \end{aligned} \quad (5.13)$$

## 5.4 Optimal trajectory

The optimization problem (5.13) can be solved with solvers for nonlinear problems. Here, a brute force optimization is done to display the impact of all variables.

The coherence bandwidth  $k_{0,5}$  and the buffer time  $T_{\text{buffer}}$  are calculated for the following variations, see Figure 12 (each grid point represents a set of variables):

- The number of points  $n_p$  is set to 3, 6, and 9.
- The radius  $r$  is chosen to 0.3, 0.4, and 0.5.
- The first distance  $x_{1,\mathcal{L}}$  varies from  $0.5D$  to  $0.75D$ .
- The spacing  $\Delta x_{\mathcal{L}}$  takes values from  $0.1D$  to  $0.2D$ .

In total, 225 different setups are evaluated. For all calculations, the following additional parameters were used:

- The preview time is chosen to  $\tau = 0.2$  s based on the pitch actuator dynamics.
- A spacing of 6 m is used for the Cartesian grid to calculate  $S_{RR}$  and  $S_{RL}$ .
- All coherences, auto- and cross spectra are calculated for  $n_f = 512$  frequencies with a discretization of  $\Delta f = \frac{1}{256}$  Hz.
- A mean wind speed of  $\bar{u} = 15$  m/s is chosen, since higher wind speeds are very unlikely in Grevesmühlen.

If the constraints are ignored, then the best of the considered setups (•) is the circle with the highest number of points (9), the largest normalized radius (0.5), and all measurement distances as close as possible to the rotor. Since, the setup is at the border of the considered optimization values, the optimal solution is likely outside of the considered ranges. However, with the solution of the unconstrained optimization, the filtered signal of the rotor effective wind speed will be around 1 s too late. For the constrained optimization, only the buffer time needs to be non-negative, since the other constraints are fulfilled by choosing the optimization variables within their limits. In this case, the optimal setup (•) is the circle with 6 measurement points, a normalized radius of 0.4 (corresponding to a half opening angle of 21.8 deg, the first distance  $x_{1,\mathcal{L}}$  at  $0.625D = 68.125$  m, and a spacing  $\Delta x_{\mathcal{L}}$  of  $0.125D = 13.625$  m. This scan configuration is displayed in Figure 11.

## 5.5 Validation of Results

The optimized trajectory has been tested in the environment described in Section 3. Tentatively the acquisition time was reduced to  $T_{\text{ACQ}} = 0.8$  s corresponding to an average over 10000 pulses in contrast to the 12000 pulses of the measurements in Section 4. However, this reduced the availability of the lidar system to 95 %. The data was processed on-line with an additional PC and measurements with a CNR below  $-22$  dB were removed. The average in Equation (5.7) was done over the remaining data. The resulting lidar estimate of the rotor effective wind speed  $v_{0L}$  has been recorded together with the data from the wind turbine and the meteorological mast using a sampling frequency of 50 Hz.

On the 17<sup>th</sup> of March 2014, data during 3 h from 10 a.m. to 1 p.m. has been collected. The basic data

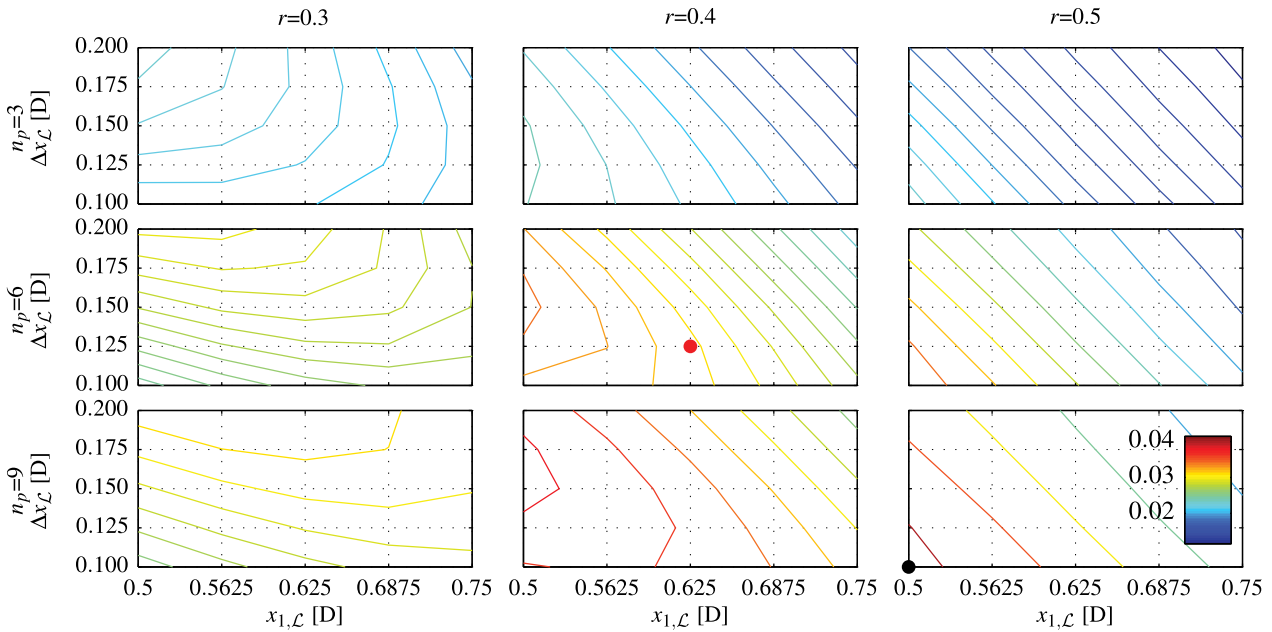


Figure 12: Coherence bandwidth depending on optimization variables. Solution of constrained (•) and unconstrained problem (•).

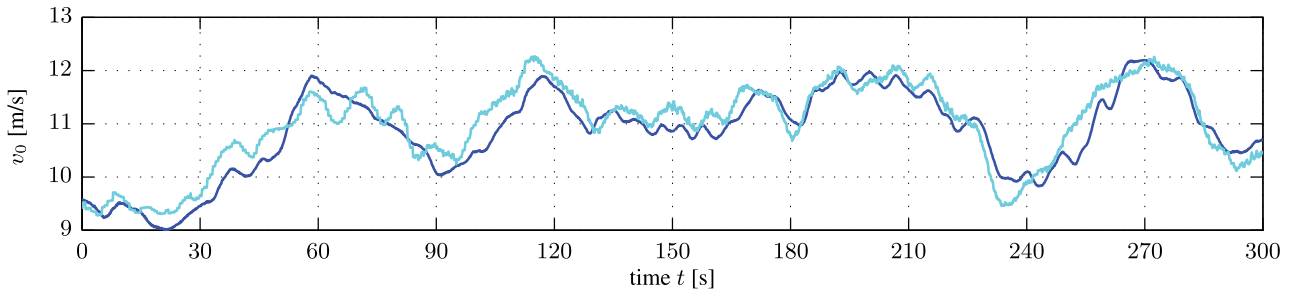


Figure 13: Lidar (—) and turbine (—) estimate of the rotor effective wind speed. First 5 min of the 3-hour-block (details see Table 4).

Table 4: Basic parameters of the evaluated 3-hour-block from the 17<sup>th</sup> of March 2014.

mean wind speed $\bar{u}_{s,w}$	mean turbulence intensity	nacelle yaw position	mean yaw misalignment $\alpha_H$
[m/s]	[-]	[deg]	[deg]
11.6	14.3	258	0.4

can be found in Table 4 and a 5 min period is shown in Figure 13. The turbine was running in normal operation.

In order to experimental evaluate the predicted correlation  $\gamma_{RL}^2$ , the rotor effective wind speed  $v_{0L}$  from the lidar is compared to the rotor effective wind speed  $v_0$  experienced by the turbine. This signal is estimated from the turbine data by an estimator similar to the one presented by VAN DER HOOFT and VAN ENGELEN (2004), because in contrast to simulations, the real wind field is unknown. With measured data of the rotor speed  $\Omega$  and the electrical power  $P_{el}$ , the aerodynamic torque  $M_a$  can be calculated using Equation (2.13). Due to numerical

issues, Equation (2.15) is reorganized into:

$$\lambda^3 = \frac{1}{2} \rho \pi R^5 \frac{c_P(\lambda, \theta)}{M_a} \Omega^2. \quad (5.14)$$

Because of the  $\lambda$ -dependency of the power coefficient  $c_P$ , an explicit expression cannot be found. The equation is solved with a set of  $M_a$ ,  $\Omega$  and the collective pitch angle  $\theta$ . With the solutions, a three-dimensional look-up table  $v_0(M_a, \Omega, \theta)$  is generated. Figure 14 shows the table at rated rotor speed from Table 1. The values are normalized by the aerodynamic torque  $M_{a,rated}$  at rated wind speed  $v_{rated}$  and the collective pitch angle  $\theta_{cutout}$  at the cutout wind speed  $v_{cutout}$ . The look-up table is then used to get a time series of  $v_0$  by a three-dimensional interpolation. All signals from the wind turbine are filtered with zero-phase notch filters at dominant frequencies of the turbine structure prior to the calculation.

In Figure 13, the preview of the lidar estimated  $v_{0L}$ , the correlation in low frequencies and the uncorrelated higher frequencies can be noted. With both signals, the coherence  $\gamma_{RL}^2$  is estimated using Welch’s averaged periodogram method with the same parameters as in Section 4 and displayed in Figure 15. The estimated coher-

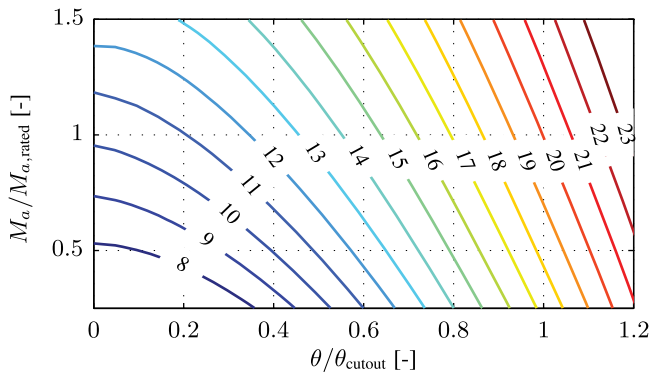


**Figure 14:** Contour lines of rotor effective wind speeds at rated rotor speed  $\Omega = 12.8$  rpm for the KENERSYS K110 turbine. For each actual set of rotor speed  $\Omega$ , pitch angle  $\theta$  and aerodynamic torque  $M_a$ , the actual wind speed  $v_0$  is interpolated.

ence is then compared to the modeled coherences using the overall correlation model described above combined with following wind evolution models:

- Wind evolution presented by KRISTENSEN (1979), using the hub height  $z_H$  as length scale and the turbulence level from Table 4.
- No wind evolution (by setting the longitudinal decay parameter  $\alpha$  to zero): the decay in correlation is only due to the combined effect of limitation to line-of-sight wind speeds, limited measurement positions and volume measurement.
- Exponential wind evolution using the longitudinal decay parameter  $\alpha = 0.2$  as identified in Section 4 and used in the trajectory optimization.
- Exponential wind evolution using the longitudinal decay parameter  $\alpha = 0.4$  as estimated based on previous work (SCHLIPF and CHENG, 2013).

Although the shape of the coherence differs slightly from the model, the estimated coherence bandwidth (wavenumber at  $\gamma_{RL}^2 = 0.5$ ) is close to the modeled one using the exponential wind evolution with  $\alpha = 0.2$ . With the longitudinal decay parameter  $\alpha = 0.4$  or using the KRISTENSEN (1979)-model, the correlation model under- or over-estimates the coherence, respectively.

The good agreement of the coherence indicates not only, that the wind evolution in this specific environment can be described by the exponential wind evolution with  $\alpha = 0.2$ , but also, that the overall model reproduces the behavior of the correlation and therefore is a promising tool to optimize the configuration for a lidar system to assisted feedforward control. The results are a strong argument, that the used trajectory is close to the optimum. However, more data is necessary to confirm the results.

In addition to the coherence, the estimated transfer function  $G_{RL}$  from the data is compared to the one modeled with  $\alpha = 0.2$  in Figure 16. Again, the shape of the estimated  $G_{RL}$  slightly differs from the modeled one, but is close to the filter, which is fitted to the modeled maximum wavenumber of  $\hat{k} = 0.03$  rad/m. Therefore, most of the uncorrelated frequencies can be filtered out

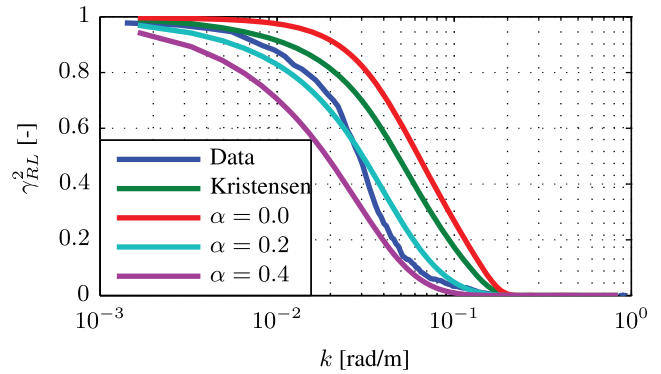


**Figure 15:** Estimated coherences between lidar and the turbine data compared with the modeled coherence without wind evolution, based on the exponential wind evolution model with different longitudinal decay parameter and the model from KRISTENSEN (1979).

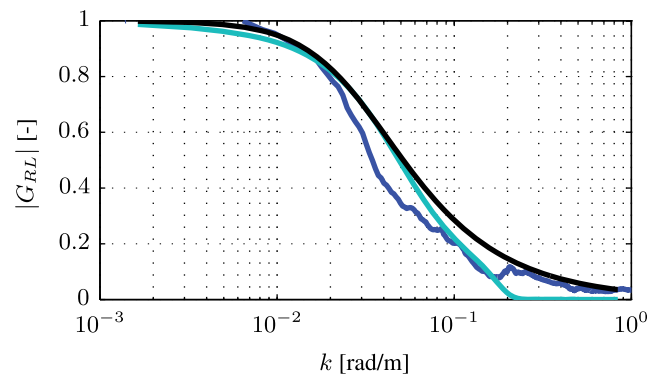


**Figure 16:** Magnitude of the estimated transfer function between lidar and turbine data (—) compared with the transfer function based on the exponential wind evolution model with a longitudinal decay parameter  $\alpha = 0.2$  (—). Fitted first-order filter (—).

without decreasing the possible benefit of lidar-assisted control by filtering too conservatively.

## 6 Conclusions and outlook

The primary contribution of this paper is the investigation of longitudinal wind evolution in the inflow of a large commercial wind turbine with a scanning lidar system installed on its nacelle. The paper illustrates that the longitudinal decay along the main wind direction cannot be identified directly with the given instrumentation. As a solution to this, an exponential coherence model of longitudinal decay is coupled with the lateral decay from the Kaimal turbulence model to account for changing wind direction. Additionally, the model is combined with a lidar measurement model to account for lidar volume measurements and the limitation to line-of-sight wind speeds. By fitting the extended coherence model to lidar measurement data, the longitudinal decay parameter is identified to be close to 0.2. However, the investigation is very sensitive to the wind direction. Further collection of lidar data is necessary to identify, if and how the wind evolution depends on additional parameters such as the atmospheric stability.

A secondary contribution of this paper is the detailed description and evaluation of an approach, which optimizes a lidar system configuration for lidar-assisted collective pitch control. Based on previous work and the wind evolution identified in the first part of the paper, a constrained optimization problem is formulated and solved. The scanning pattern of the installed lidar system is optimized such that it provides a wind speed signal, which on the one hand exhibits a high correlation to the wind speed affecting the turbine in order to improve the control performance. On the other hand, the problem considers, that the signal needs to be transferred to the control system with enough preview to filter out the uncorrelated frequencies, which have negative impacts on structural loads. As a measure of the correlation, the coherence bandwidth is used, which is the wavenumber, where the magnitude squared coherence reaches a value of 0.5. The optimized lidar scan configuration was tested on a large commercial wind turbine. The modeled and measured coherence show good agreement. This validates the identified wind evolution parameter and the overall approach. More data needs to be collected with the optimized scan configuration and suboptimal scans, to further confirm the results. The paper presents, that distributing evenly as many measurements as possible over the rotor disk between 0.5 and 1 rotor diameter provides the best correlation. However, the timing constraint might require, that fewer measurements need to be taken at distances over 0.5 rotor diameter.

The optimized trajectory has been tested with feed-forward collective pitch control. Future work will evaluate the structural loads to estimate the benefit of the lidar-assisted collective pitch control. Further, an extension of the correlation model for wind shears is planned to assisted individual pitch control.

## Acknowledgments

The authors thank all who are involved in the ongoing control campaign. Thanks to FIONA DUNNE and ERIC SIMLEY for the valuable discussions.

Part of this research is funded by the German Federal Ministry for Economic Affairs and Energy (BMWi) in the framework of the German joint research projects “LIDAR II” and “LIDAR Complex”. This work was supported by the German Research Foundation (DFG) within the funding programme Open Access Publishing.

## References

- BENDAT, J.S., A.G. PIERSOL, 2012: Random data; analysis and measurement procedures – John Wiley & Sons, Inc., New York, USA.
- BOSSANYI, E., 2012: Un-freezing the turbulence: improved wind field modelling for investigating lidar-assisted wind turbine control. – In: Proceedings of the European Wind Energy Association annual event, Copenhagen, Denmark.
- CARIOU, J.-P., 2013: Pulsed lidars. – In: Remote Sensing for Wind Energy, DTU Wind Energy-E-Report-0029(EN), chapter 5, 104–121.
- CARTER, G.C., C. KNAPP, A.H. NUTTALL, 1973: Estimation of the magnitude-squared coherence function via overlapped fast fourier transform processing. – IEEE Trans. Audio **21**, 337–344.
- DUNNE, F., L.Y. PAO, D. SCHLIPF, A.K. SCHOLBROCK, 2014: Importance of lidar measurement timing accuracy for wind turbine control. – In: Proceedings of the American Control Conference, Portland, Oregon, USA.
- HAU, E., 2006: Wind Turbines: Fundamentals, Technologies, Application, Economics. – Springer Science & Business Media, 897 pp.
- IEC 61400-1, 2005: Wind turbines - Part 1: Design requirements.
- KRISTENSEN, L., 1979: On longitudinal spectral coherence. – Bound.-Layer Meteor. **16**, 145–153.
- LAKS, J., E. SIMLEY, L.Y. PAO, 2013: A spectral model for evaluating the effect of wind evolution on wind turbine preview control. – In: Proceedings of the American Control Conference, Washington, DC, USA.
- MANN, J., 1994: The spatial structure of neutral atmospheric surface-layer turbulence. – J. Fluid Mech. **273**, 141–168.
- PIELKE, R.A., H.A. PANOFKY, 1970: Turbulence characteristics along several towers. – Bound.-Layer Meteor. **1**, 115–130.
- RAACH, S., D. SCHLIPF, F. HAIZMANN, P.W. CHENG, 2014: Three dimensional dynamic model based wind field reconstruction from lidar data. – J. Phys. Conference Series **524**, 012005.
- RETTENMEIER, A., J. ANGER, O. BISCHOFF, M. HOFSSÄSS, D. SCHLIPF, I. WÜRTH, 2013: Nacelle-based lidar systems. – In: Remote Sensing for Wind Energy, DTU Wind Energy-E-Report-0029(EN), chapter 8, 157–170.
- SCHLIPF, D., in review: Lidar-Assisted Control Concepts for Wind Turbines. – Ph.D. thesis, University of Stuttgart.
- SCHLIPF, D., P.W. CHENG, 2013: Adaptive feed forward control for wind turbines. – AT-Autom. **61**, 329–338.
- SCHLIPF, D., J. MANN, P.W. CHENG, 2013a: Model of the correlation between lidar systems and wind turbines for lidar assisted control. – J. Atmos. Ocean. Technol. **30**, 2233–2240.
- SCHLIPF, D., D.J. SCHLIPF, M. KÜHN, 2013b: Nonlinear model predictive control of wind turbines using LIDAR. – Wind Energy **16**, 1107–1129.
- SCHLIPF, D., P. FLEMING, F. HAIZMANN, A. SCHOLBROCK, M. HOFSSÄSS, A. WRIGHT, P.W. CHENG, 2014: Field testing of feedforward collective pitch control on the CART2 using a nacelle-based lidar scanner. – J. Phys. Conference Series **555**, 012090.
- SCHOLBROCK, A., P. FLEMING, L. FINGERSH, A. WRIGHT, D. SCHLIPF, F. HAIZMANN, F. BELEN, 2013: Field testing LIDAR based feed-forward controls on the NREL controls advanced research turbine. – In: Proceedings of the 51st AIAA Aerospace Sciences Meeting Including the New Horizons Forum and Aerospace Exposition, Dallas, USA.
- SIMLEY, E., L.Y. PAO, 2013a: Correlation between rotating LIDAR measurements and blade effective wind speed. – In: Proceedings of the 51st AIAA Aerospace Sciences Meeting Including the New Horizons Forum and Aerospace Exposition, Dallas, USA.
- SIMLEY, E., L.Y. PAO, 2013b: Reducing lidar wind speed measurement error with optimal filtering. – In: Proceedings of the American Control Conference, Washington, DC, USA.
- SIMLEY, E., L.Y. PAO, N. KELLEY, B. JONKMAN, R. FREHLICH, 2012: LIDAR wind speed measurements of evolving wind fields. – In: Proceedings of the 50th AIAA Aerospace Sciences Meeting Including the New Horizons Forum and Aerospace Exposition, Nashville, USA.
- TAYLOR, G.I., 1938: The spectrum of turbulence. – P. Roy. Soc. Lond. A Mat. **164**, 476–490.
- VAN DER HOOFT, E., T.G. VAN ENGELEN, 2004: Estimated wind speed feed forward control for wind turbine operation optimization. – In: Proceedings of the European Wind Energy Conference, London, UK.